

# Rapid Prototype Development and Demonstration of a Frequency-Multiplexed Phased-Array Antenna System

Spyro Gumas, Ravi P. Goonasekeram, Timothy A. Sleasman, John A. Marks, and David W. Elsaesser

## ABSTRACT

A phased array is a directive, electronically steered antenna consisting of multiple antenna elements wherein each element's signal has a unique phase shift applied so that the combined phase-shifted contributions from each element form an antenna beam in the desired direction for both transmission and reception. Phase shifting and beam formation had been performed using analog components outside of the radio transceiver until the advent of digital signal processing introduced digital beamforming. With digital beamforming, the signal from each antenna element is connected directly to an analog to digital converter (ADC) input of a multichannel transceiver. The phase shifting and combining is performed during the digital processing, allowing for fast beam hopping and complex beam pattern generation. However, multiple ADCs can be costly in terms of size, weight, and power (SWaP) and overall complexity, particularly as the number of elements in the phased array increases. This article describes the development, fabrication, and testing of a new type of digital beamforming phased-array antenna system by researchers at the Johns Hopkins University Applied Physics Laboratory (APL). The system frequency-multiplexes the signal from multiple antenna elements onto a single analog line, offering potential solutions for applications where cost and size are of concern. This system can also operate as a coherent multichannel transceiver, offering similar cost and size savings. This project, which progressed from concept to hardware to successful field testing in less than a year, exemplifies the results that APL—leveraging its multidisciplinary teams, world-class engineering expertise, and state-of-the-art fabrication facilities—is able to achieve.

## INTRODUCTION

This article describes the frequency-multiplexed phased array (FMPA) that an APL team developed and prototyped as a proof of concept for a new phased-array antenna system. The system's individual antenna channels are frequency-multiplexed onto a single analog

channel that feeds a conventional single-channel digital transceiver. This effort included development of a receive-only capability, but the approach is directly applicable to a transmit capability as well. For simplicity, this article adopts a receive-only perspective.

The FMPA system can also be operated as a coherent multichannel transceiver (CMCT). When the system operates as a CMCT, each antenna channel is assigned a unique and independent center frequency. The frequency segments covered by all the antenna channels are then multiplexed onto a single analog channel fed into the transceiver. The CMCT can thereby cover a large noncontiguous frequency range. The CMCT capability is an additional benefit of the FMPA development and is briefly discussed at the end of this article.

The four-member core APL team on this project has more than 10 years of experience working together on similar breakthrough challenges. Members' expertise includes radio frequency (RF) system modeling and validation, hardware design prototyping and characterization, firmware development, electronics and mechanical prototyping, system integration, functional verification, and range and flight testing. This small team, with its wide-ranging expertise, afforded agile, rapid, and cost-effective development and demonstration of this novel capability.

## BACKGROUND

### Traditional Phased Array with Analog Receiver

The signal flow for a traditional phased-array antenna receiver is depicted in Figure 1. Multiple ( $N$ ) antenna elements receive the signal. Each antenna channel's signal independently undergoes phase rotation in the analog domain. After phase rotation, the signal channels are combined and summed into an analog composite signal. Beam steering is performed by changing the amount of phase rotation applied to individual antenna channels. The analog composite signal is then fed into the analog input of the receiver.<sup>1</sup>

With a traditional phased array with an analog receiver, the ability to change the beam steering pattern in real time depends on the ability to change the phase

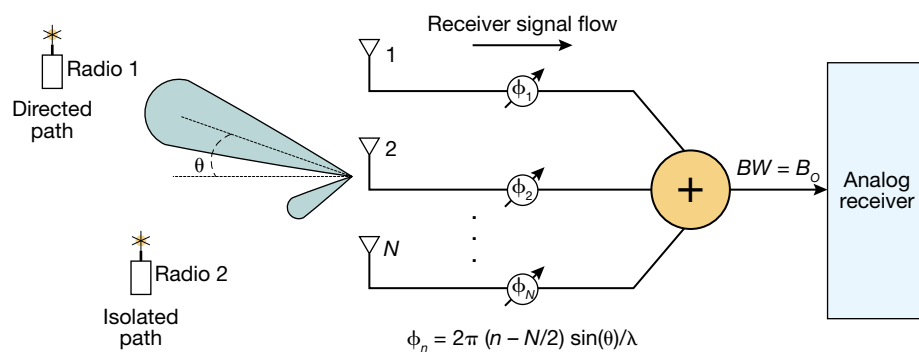


**Figure 1.** Traditional phased array with analog receiver. In this configuration, several ( $N$ ) antenna elements receive the signal, and each antenna channel's signal independently undergoes phase rotation in the analog domain. The channels are then combined and summed, and different amounts of phase rotation are applied to individual antenna channels to steer the beams. Finally, the analog composite signal is fed into the analog input of the receiver.

coefficient on each analog phase rotation element in real time. Depending on the design of the phase rotation element, the phase coefficient is fixed, manually reconfigurable, or electronically reconfigurable. This design choice determines the system's flexibility in terms of real-time beam steering.<sup>2</sup>

This architecture is limited to the beam patterns used when the signals were collected. Any recordings of the received composite analog signal will already have a specific beam pattern imprint that cannot be changed. Thus, any playback of recorded data will not allow for different beam steering, interference nulling, or beam pattern experimentation in general.

The traditional system must provide phase calibration for each signal path from the antenna to the receiver. This calibration accounts for the nonuniform accumulation of phase change through the electronics of each channel and along each channel's signal path as a function of temperature and frequency caused by long cable runs between the antenna and receiver.

### Traditional Phased Array with Digital Signal Processing Receiver

The signal flow for a traditional phased array with a digital receiver is shown in Figure 2. The signal from each antenna element goes through a channel conditioner, which prepares the signal for digital processing. Channel conditioning typically includes amplification, RF down-conversion, and filtering. Each conditioned signal is then fed into one of the  $N$  analog-to-digital converter (ADC) inputs of a digital signal processing receiver, often referred to as a software defined radio (SDR).

Within the SDR, phase rotation is applied in the digital domain to the signal collected from each  $N$  antenna element independently. After phase rotation, the signal channels are combined and summed into a digital composite signal. Beam steering is performed by changing

the amount of phase rotation each individual antenna channel undergoes.<sup>3</sup> As with the analog receiver, phase calibration is required for each signal path from the antenna because of the non-uniform phase change along each signal path.

This architecture offers the advantage of multiple simultaneous beams, often in real time. This capability is possible because the phase coefficients are internal digital processing parameters that are easily accessible and reconfigurable by the

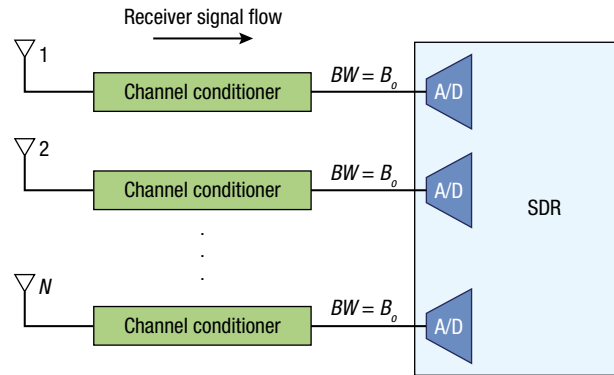


**Figure 2.** Traditional phased-array system with SDR. The signal from each antenna element goes through a channel conditioner, and then each conditioned signal is fed into one of the  $N$  ADC inputs of a digital signal processing receiver, or SDR. Within the SDR, phase rotation is independently applied in the digital domain to the signal collected from each of the  $N$  antenna elements. After phase rotation, the  $N$  signal channels are combined and summed into a digital composite signal, and the amount of phase rotation each individual antenna channel undergoes is changed to steer the beams.

processor. Multiple independent processing threads can be established to support multiple beams. Additionally, any recordings of the received digitized channels can be played back with different beam patterns applied. Thus, any playback of recorded data can use alternative beam steering, interference nulling, or beam pattern experimentation in general.

While this architecture offers benefits in real-time beam steering and significant flexibility during data playback, it adds cost in terms of size, weight, and power (SWaP) and overall complexity because it requires a multichannel digital signal processing receiver.

### Overview of FMPA Receiver

The FMPA receiver provides most of the benefits of a traditional phased array with a digital receiver, but with a potentially more cost-effective and flexible hardware architecture. The signal flow for the FMPA receiver is shown in Figure 3. The signal from each antenna element goes through a tunable analog downconverter that has a filter pass bandwidth of  $B_0$  and an adjustable downconversion frequency of  $F_0$ . Each of the  $N$  channels is downconverted to a unique frequency at least  $B_0$  away from its adjacent channels. After downconversion, all  $N$  analog channels are combined into a single analog composite signal of bandwidth greater than or equal to  $N \times B_0$  such that there is little to no spectral overlap among the  $N$  channels. This analog composite signal comprises the frequency-multiplexed signals from  $N$  antenna channels, and it is fed into the ADC input of an SDR.

Within the digital signal processing implemented in the SDR, frequency demultiplexing separates the

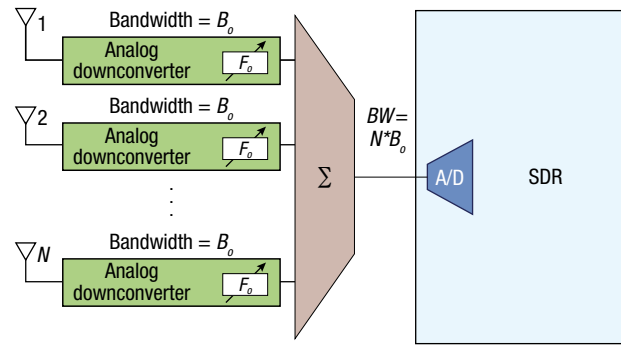


**Figure 3.** FMPA system with SDR. In this architecture, the signal from each antenna element is downconverted to a unique frequency at least  $B_0$  away from its adjacent channels. Then all analog channels are combined into a single analog composite signal such that there is little to no spectral overlap among the channels. This analog composite signal, which comprises the frequency-multiplexed signals from  $N$  antenna channels, is fed into the ADC input of an SDR. Within the SDR, frequency demultiplexing separates the  $N$  channels, and then phase rotation is applied to each signal channel independently. Finally, all the signal channels are summed to form a digital composite signal, and the amount of phase rotation that each channel undergoes is changed to steer the beams.

channels. Then phase rotation is applied in the digital domain to each signal channel independently. After phase rotation, all the signal channels are summed to form a digital composite signal. Beam steering is performed by changing the amount of phase rotation that each channel undergoes.

The benefits of FMPA are best contextualized as a functionality trade-off between an FMPA receiver and a traditional phased array with a digital receiver. For  $N$  antenna elements and a target signal of bandwidth  $B_0$ , the FMPA requires only one ADC; however, it requires a minimum digitizing bandwidth of  $N \times B_0$ . On the other hand, a traditional phased array with a digital receiver requires  $N$  ADCs; however, each only requires a minimum digitizing bandwidth of  $B_0$ .

A traditional phased array with a digital receiver provides one unique advantage over FMPA:

- It requires  $N$  ADCs; however, each requires only a minimum digitizing bandwidth of  $B_0$ . At some point as target signal bandwidth  $B_0$  increases, an FMPA receiver capable of processing a single  $N \times B_0$  data stream may be more expensive and complex than a traditional phased array with a digital receiver.

An FMPA receiver and a traditional phased array with a digital receiver share some advantages:

- Both offer agile, real-time, post-digitization beam steering. The antenna phase coefficients are internal processing parameters that are easily accessible and reconfigurable by the processor.

- Since phase coefficients are applied within the signal processor after digitization, both architectures enable recording of the digitized data stream. Recorded data can then be played back with alternative beam patterns applied, thereby enabling iterative trials using alternative beam steering, interference nulling, or any other beam pattern manipulation.
- Multiple processors can share the digitized stream (FMPA) or streams (traditional) of antenna data and perform independent, concurrent beam steering functions.

An FMPA receiver offers unique potential advantages over a traditional phased array with a digital receiver:

- It requires only a single-channel digital receiver, which is inexpensive and readily available in the form of SDRs. Whether or not this is truly an advantage for an FMPA over a traditional phased array with a digital receiver depends on the design implementation details of each approach in satisfying the specific system-imposed requirements.
- It simplifies the maintenance of phase calibration. Because an FMPA receiver can place the down-converters and summing combiner near the actual antenna elements, only a single analog cable connects the antenna to the SDR. This avoids the nonuniform accumulation of phase change along multiple ( $N$ ) long cable runs on other systems.

To explore these potential advantages in an existing single-channel SDR application, APL developed and prototyped an FMPA system. The effort included three main thrusts: FMPA algorithm modeling and simulation, prototype hardware development, and system testing, each of which is described in more detail in the following sections.

## FMPA SIMULATION TEST BED

APL developed a test bed to simulate FMPA receiver performance. The test bed performed four fundamental tasks: synthetic target generation, front-end simulation, FMPA simulation, and signal analysis. Figure 4 details the test bed and defines the functionality.

The synthetic target simulator was developed to model targets in the far field. It generates the signals going from the target to each  $N$  antenna element using a plane wave model of the signal at the antenna interface and applying path-length-appropriate phase rotation for each antenna channel signal. The complex conjugates of the phase coefficients computed here form the array factor coefficients used later in the FMPA simulator.

Two targets were simultaneously presented to the test bed to investigate FMPA performance of directing a beam at a desired target while simultaneously rejecting

interference from an off-beam target. Additionally, two types of targets were investigated:

1. Continuous wave (CW) targets were synthesized and used to make antenna beam gain measurements and to determine the isolation or rejection of the off-beam interferer.
2. Two data-encoded quadrature phase shift keying (QPSK)-modulated targets were synthesized on the same carrier frequency with different data payloads. These were used to verify that a cofrequency interferer could be rejected while still receiving the data payload from the desired transmitter.

The front-end simulator was developed to model the analog electronics starting at the antenna element interface and extending to the ADC.

The FMPA simulator receives the  $N$  channel frequency-multiplexed signal and implements the algorithm and calculations for frequency-multiplexed phased-array processing.

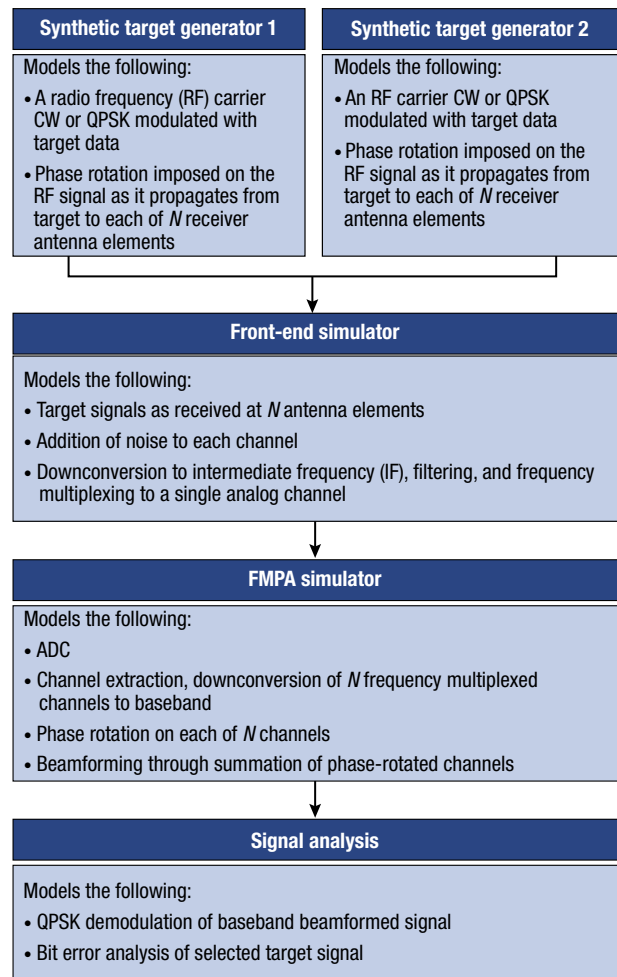


**Figure 4.** FMPA simulation test bed. The test bed performed four fundamental tasks: synthetic target generation, front-end simulation, FMPA simulation, and signal analysis.

Signal analysis evaluates the FMPA simulation performance, from synthetic target generation to beamformed baseband signal generation. Two classes of synthesized targets were evaluated: CW tones and data-encoded QPSK-modulated signals. For this analysis, the FMPA system was modeled with 16 antenna elements in a linear array with a bandwidth ( $B_o$ ) of 10 MHz.

### Analysis Using Two CW Targets

The two CW targets were modeled, each as a narrow CW tone, with a spacing between the two targets of 1 MHz. The array factor was calculated such that the beam points directly at target 1 at antenna broadside. The predicted phased-array beam response profile was computed and used as a template to compare the relative signal strength contribution from each of the two CW targets. This was done by moving the position of target 2 across several locations on the predicted beam response profile. Two metrics were assessed for this evaluation:

1. The signal rejection of target 2 relative to target 1. These values were compared to the predicted beam response profile. The results are plotted in Figure 5 and quantified in Figure 6.
2. The signal-to-noise ratio (SNR) improvement resulting from coherent integration of  $N$  antenna channels. Noise was injected onto each channel to achieve an SNR of 40 dB before beam formation. After beam formation, the SNR for target 1 is 52 dB, or 12 dB greater than before beam formation. This tracks with the expected integration gain for a 16-element phased-array antenna,  $10\log(16) = 12$  dB. These simulation results are also shown in Figure 6.

### Analysis Using Two QPSK Targets

Data-encoded waveforms were synthesized and fed through the FMPA test bed to verify FMPA performance in spatially rejecting a co-channel interfering signal (a signal on exactly the same frequency). The

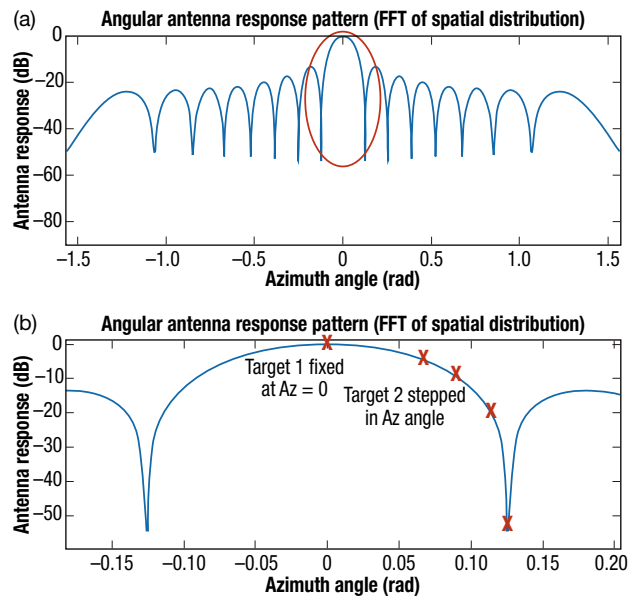
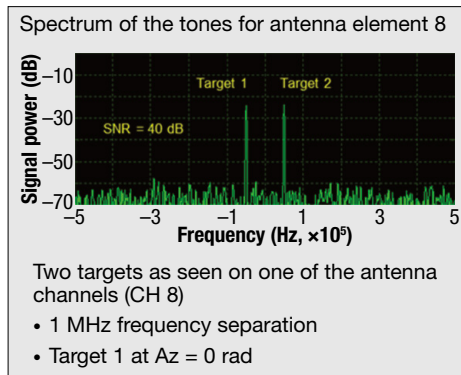


**Figure 5.** Relative signal strength contribution from each of the two CW targets. (a) Predicted beam response profile and (b) magnified view of red-circled portion showing normalized response of target 1 and corresponding response of target 2 as it is stepped across four unique angles. FFT, fast Fourier transform.



Azimuth (rad)	Predicted Rejection (dB)	Simulated Rejection (dB)
0.070	5.0	5.1
0.093	10.0	10.2
0.114	20.0	20.5
0.125	>50.0	>50.0

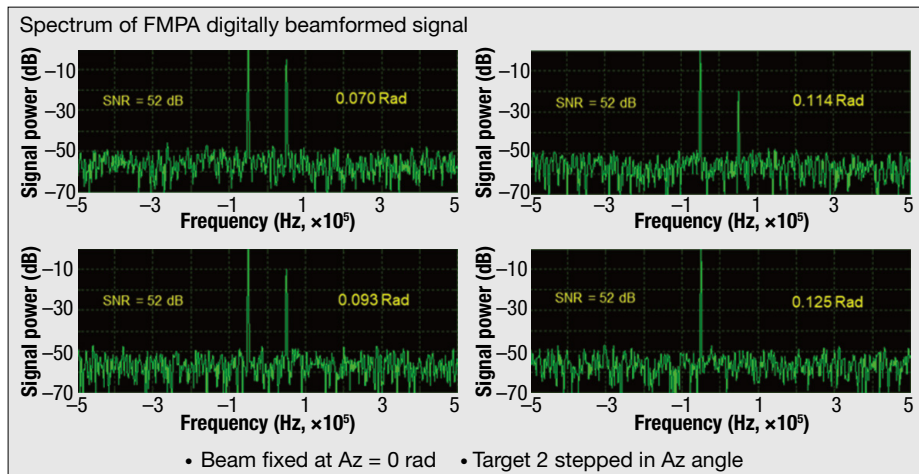


**Figure 6.** Simulation results. Top, Power spectrum of target 1 and target 2 on a single antenna channel. Bottom, Power spectrum of targets 1 and 2 after beam formation while target 2 is stepped in increasing azimuth angle.

data-encoded targets were modeled as two independent QPSK-modulated signals sharing the same carrier frequency so that each served as an interferer for the other. The two QPSK signals also shared the following common parameters: symbol rate ( $S_r$ ) = 1 MHz, message length (NumBits) = 120 bits, and Gaussian pulse filtering  $\alpha = 3.5$ .

The target 1 and target 2 QPSK-modulated signals were modeled at two different azimuth angles and modulated with two different ASCII messages to differentiate them during detection, after beam formation. Target 1 had an ASCII data payload of “\_Hello\_World\_” and an off-boresight azimuth angle ( $\phi$ ) =  $-0.30$  rad, while target 2 had an ASCII data payload of “Drink More Beer” and  $\phi = +0.48$  rad.

The azimuth angles for the two targets were selected so that when the beam was formed at one target, the other target would reside in an antenna pattern null, with a resulting rejection ratio of greater than 40 dB. This is shown in Figure 7.

### Simulation Results—Single QPSK Transmitter, Target 1

A single transmitter, target 1, was simulated with an azimuth angle of  $-0.30$  rad. The phased array was pointed to a  $-0.30$ -rad look angle. Noise was injected into the signal at each antenna element to yield a bit error rate (BER) of 0.01. Figure 8 shows the QPSK eye and constellation patterns for a representative antenna channel (channel 8) and the results of individual channel demodulation for all 16 antenna channels. Demodulation of the 120-bit data message “\_Hello\_World\_” is also shown in Figure 8, with an average BER across all 16 channels of  $\sim 0.008$ .

The results of beamforming on target 1 are shown in Figure 9. The eye and constellation show SNR improvement resulting from coherent integration across 16 antenna channel inputs. The message is demodulated without error.

### Simulation Results—Dual QPSK Transmitters, Target 1 and Target 2

Two transmitters, target 1 and target 2, were modeled in the simulation at azimuth angles of  $-0.30$  and  $+0.48$  rad, respectively. Noise was injected into the signal at each antenna

element to maintain the same SNR as used in the single QPSK transmitter simulation. Figure 10 shows the QPSK eye and constellation patterns for a representative antenna channel (channel 8) and the results of attempting to demodulate the individual channels for all 16 antenna channels. Individual channel demodulation failed due to co-channel interference. The two

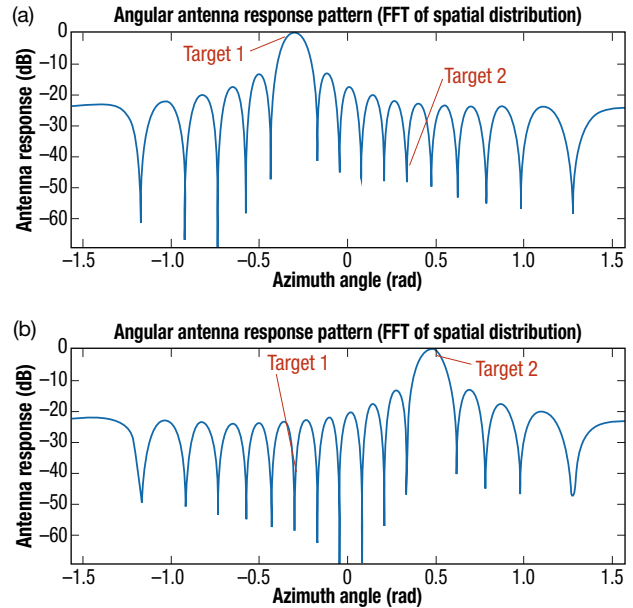


Figure 7. Analysis using two QPSK targets. Beam patterns looking at (a) target 1 at  $-0.30$  rad and (b) target 2 at  $+0.48$  rad. FFT, fast Fourier transform.

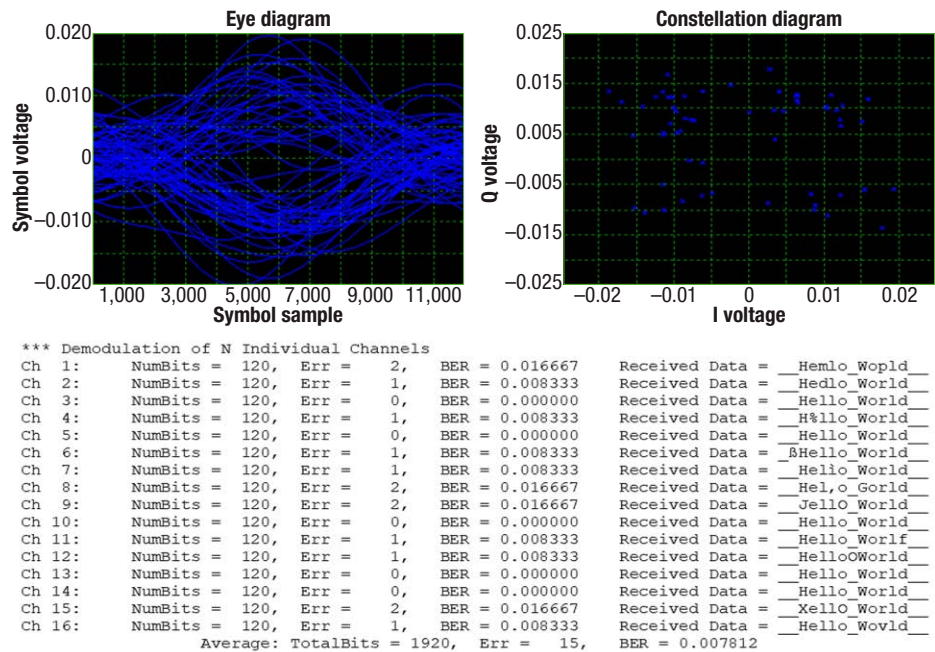
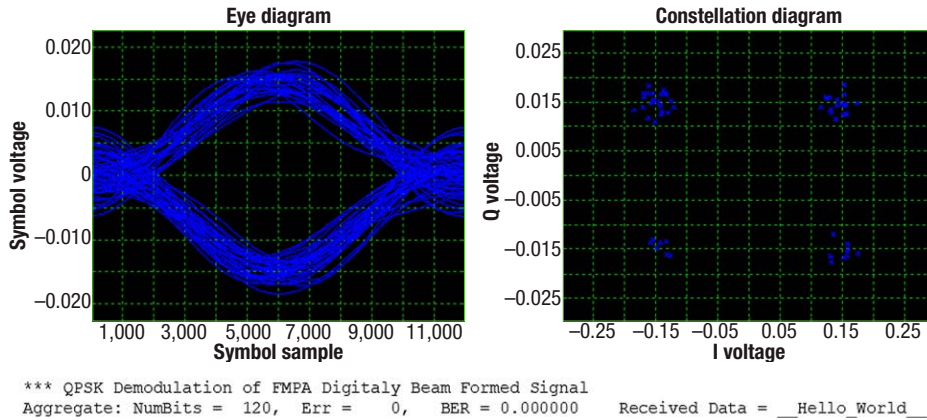


Figure 8. Simulation results. Shown are results for a single QPSK transmitter, target 1 eye and constellation patterns at antenna channel 8, as well as demodulation results for each individual antenna channel. Average BER =  $\sim 0.008$ .

strong target signals effectively jammed each other, and no valid QPSK message was demodulated and recovered. The demodulated message for each individual channel is shown in the figure, with an average BER across all 16 channels of  $\sim 0.23$ .

This simulation was run twice, once with the phased array pointing at target 1 with a  $-0.30$ -rad look angle, and again with the phased array pointing at target 2 with a  $+0.48$ -rad look angle. For this dual-transmitter

simulation, the results of beamforming on target 1 and target 2 are shown in Figure 11. Compared with Figure 10, the expanded eye and more closely grouped constellation shown in Figure 11 reflect improved SNR for the on-beam target signal and rejection of off-beam target signal. This simulation demonstrates the FMPA's ability to reject co-channel interference as long as the interferer is outside of the main beam. The amount of rejection is a function of the spatial positioning of the interfering target relative to the antenna beam pattern and sidelobes. As mentioned earlier, the spatial positioning of the two targets used in this simulation provides a theoretical rejection of greater than 40 dB between them.



**Figure 9.** Results of beamforming on target 1. Shown are eye and constellation patterns of the QPSK signal after beamforming on the target 1 location at look angle =  $-0.30$  rad. The expanded eye and more closely grouped constellation reflect improved SNR resulting from coherent integration gain across all 16 elements, with BER =  $\sim 0$ .

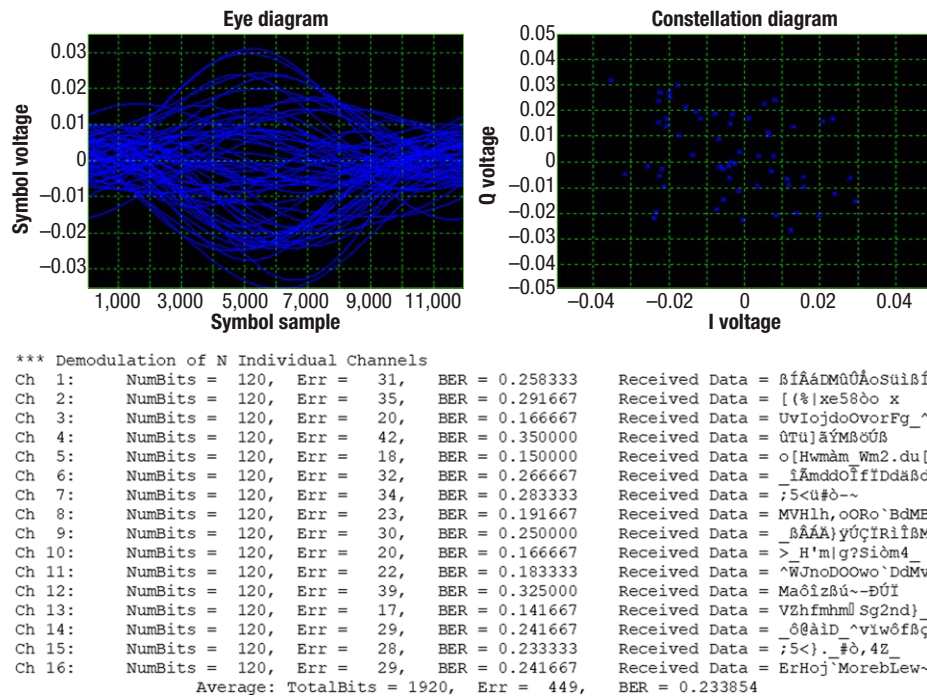


**Figure 10.** QPSK eye and constellation patterns for channel 8 and the results of attempting to demodulate the individual channels for all 16 antenna channels. Shown are dual QPSK transmitter, target 1 and target 2, eye and constellation patterns at antenna channel 8, as well as demodulation results for each individual antenna channel. Individual channel target data are not recovered because of co-channel interference.

## ANTENNA DEVELOPMENT

The antenna development process included antenna selection, design and prototyping, fabrication, and characterization. An antenna architecture was chosen for its polarization, bandwidth, and size/weight characteristics. The antenna consisted of stacked patches and a quadrature hybrid feeding scheme for the purposes of bandwidth and polarization, respectively. Fabrication and assembly was PCB-based and included adhesion with an internal foam layer. Following the development of a  $1 \times 4$  subarray, the module could be tiled to create  $1 \times 16$  and  $4 \times 4$  arrays. The resulting arrays were characterized in an anechoic chamber and found suitable for operation, covering the desired bandwidth and delivering circular polarization.

## Antenna Selection

To design and develop the antenna, we had to consider both the array performance and the characteristics of

its constituent parts. The choice of the antenna architecture was driven primarily by considerations for bandwidth, polarization, ease of fabrication, and low weight. To maintain low size and weight, a printed circuit board (PCB)-based antenna was chosen. Starting from the basic notion of a traditional patch antenna, the antenna was adapted to enhance bandwidth as necessary and the feed was designed to create a circular polarization.

Basic microstrip patch antennas tend to be narrow-band. To improve bandwidth, the substrate between the patch and the ground plane can be made thicker. Bandwidth can also be increased by using a stacked patch geometry. In this case, a single patch (close to the ground plane) is excited, and it subsequently excites a secondary patch that is farther from the ground plane. Based on the size and coupling between the patches, as well as the thickness of the substrate between, the bandwidth can be increased to cover the desired frequency range.

Likewise, there are numerous methods to achieve the desired circular polarization behavior. Circular polarization allows the antenna to couple in an appreciable amount to either of the linear polarizations, making for a robust link. A traditional patch excited at a single location can easily create a linear polarization (e.g., vertical). Exciting at a second position (mirror in location from the first) allows for the other linear polarization (horizontal) to be generated. A circular polarization can then be created by exciting both of these polarizations simultaneously with a  $90^\circ$  phase difference between the two. While this phase difference can be created with delay lines or other phase shifting techniques, a common and convenient approach is to use a quadrature hybrid coupler, which takes a single input signal, splits it in two, and

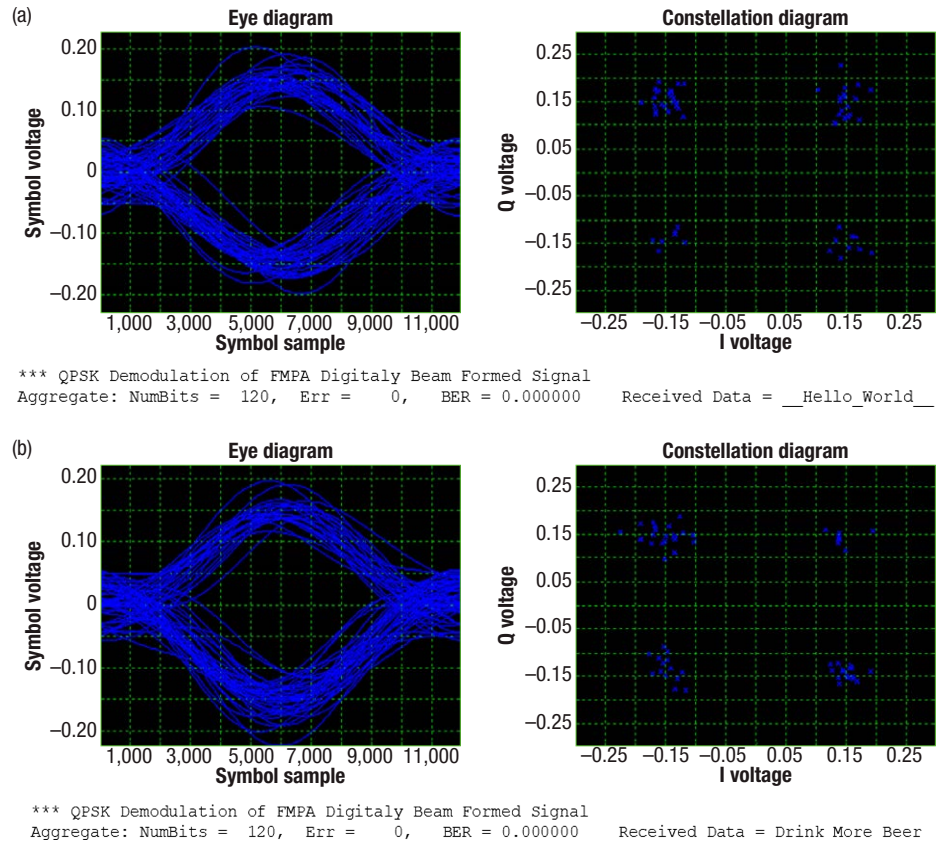


**Figure 11.** Dual-transmitter results after beam formation. (a) Beam pointing at target 1 location, look angle =  $-0.30$  rad. (b) Beam pointing at target 2 location, look angle =  $+0.48$  rad. Both target 1 and target 2 messages demodulated with BER =  $\sim 0$ .

applies a  $90^\circ$  phase shift to one branch. For each patch array element, a single coaxial connector inserts a signal, which excites each of the linear polarizations. Aperture coupling was used to excite the patch from transmission lines that are shielded below the ground plane. All of the electronics are also located behind the antenna ground plane, minimizing any possible interference.

The resulting antenna element is therefore an aperture-coupled stacked patch antenna that can be stimulated at a single feed to create a circular polarization. The element is depicted in Figure 12. The element is smaller than half of a wavelength and can therefore be

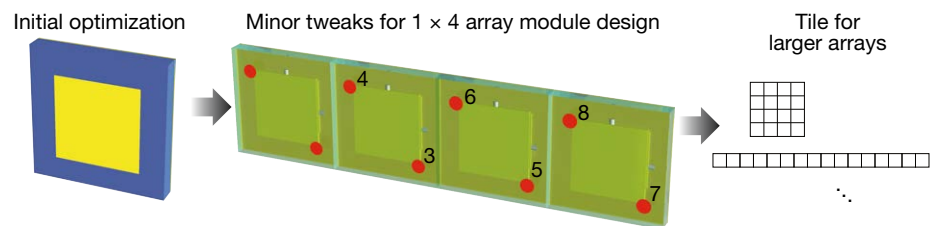


**Figure 12.** Element and tiling concept. The antenna element is an aperture-coupled stacked patch antenna that can be stimulated at a single feed to create a circular polarization. It is smaller than half of a wavelength and can therefore be arrayed without risk of severe grating lobes.

arrayed as necessary without risk of severe grating lobes. Below, the performance of an individual patch element and the arrayed antenna in multiple configurations is discussed. Ultimately, a design with a  $1 \times 4$  patch was selected to serve as a subarray module. This  $1 \times 4$  subarray could then be tiled to create a  $1 \times 16$  array or a  $4 \times 4$  array.

### Antenna Design and Prototyping

Before the prototype was built, simulations were completed on a single stacked patch element in isolation as well as on a finite array. All simulations and design studies were accomplished in CST design studio, a full-wave electromagnetic solver that can calculate radiated fields from a given antenna/array geometry.

Before the aperture-coupled patch antenna as an array was approached, a single patch with a single linear polarization was designed. This verified the manufacturing process and confirmed material properties. Because of the stacked patch geometry, one of the spacers was a structural foam with a low dielectric constant. We adhered the foam to the bottom PCB (that constitutes the feeding board) and the top PCB (that hosts the top-most patch) with an epoxy layer. We then studied the test patch with a single polarization to confirm that this fabrication process was feasible and returned realized results that tracked the performance predicted through the simulations. The test patch behaved as expected, showing the desired radiation at the correct operating frequency and with the

desired bandwidth, thereby confirming that the design flow was robust. The test patch is shown in Figure 13a.

We then designed the circularly polarized stacked patch antenna element. To host the stacked patch geometry and the requisite feeding architecture, a multi-layer stack-up was selected with two separate PCBs that sandwich a foam layer. This stack-up is shown in Figure 13b. Layers 1 and 2 (L1 and L2) each host patches with slightly different sizes. The routing/feed layer, L4, hosts microstrip transmission lines, a quadrature hybrid coupler, and the SMA connectors that inject the RF signal. An incision (a rectangular aperture) is made in the ground layer, L3, where the signal is reactively coupled from the feed layer to the patches. All these layers represent metallization planes and do not include the dielectric substrates/spacers.

The various parameters requiring optimization include the sizes of the patches, the shapes and locations of the incisions in L3, and the geometry of the transmission lines on the routing layer. The foam and PCB thicknesses (and their material properties) were selected primarily to increase bandwidth. Patch size is the most important feature for obtaining the correct operating frequency. Together with the size and location of the incision on L3 and the geometry on the feed layer (which includes impedance matching stubs), a series of coupled resonators is generated. These can all be adjusted in parallel to ensure optimal performance. These various parameters were studied in the context of a single

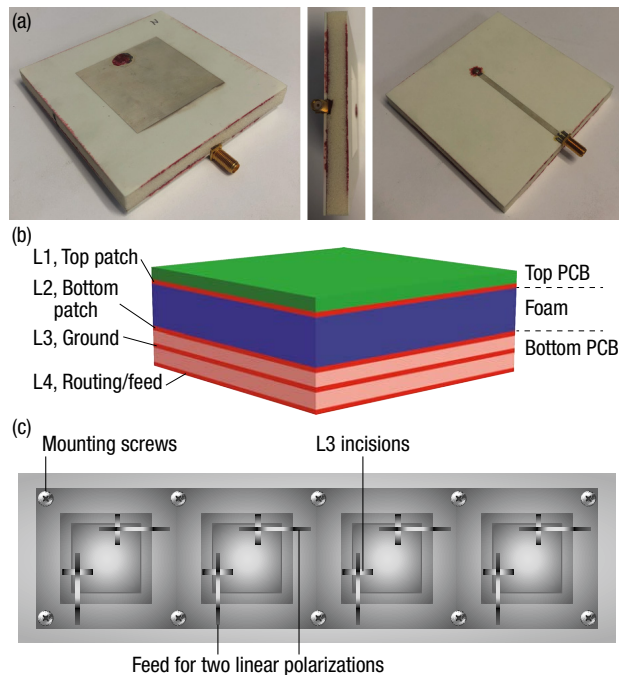


**Figure 13.** Antenna design and fabrication evolution. (a) Patch with a single element linearly polarized. (b) Multilayer stack-up for circularly polarized stacked patch. (c) X-ray view of the optimized  $1 \times 4$  array.

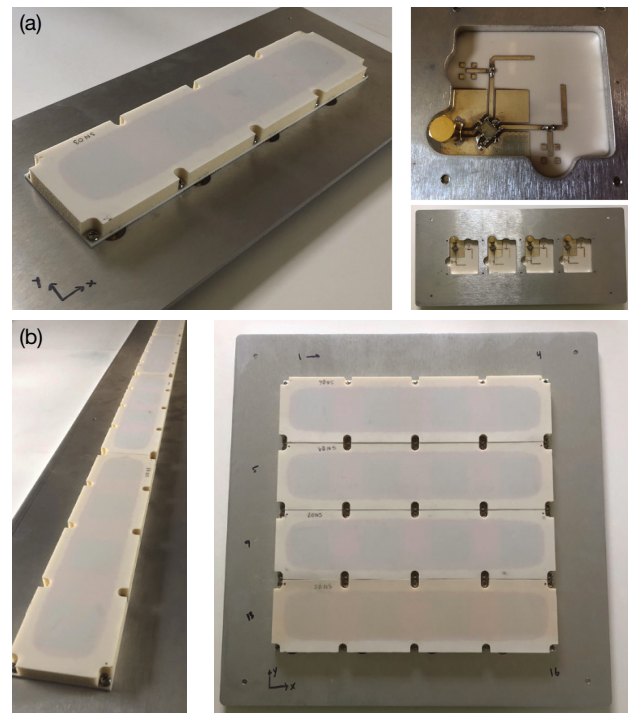


**Figure 14.** Fabricated antenna assembly. (a)  $1 \times 4$  antenna module front and rear views. (b)  $1 \times 4$  antenna modules arranged in  $1 \times 16$  and  $4 \times 4$  configuration.

element and then incorporated into a  $1 \times 4$  array. After designing the geometry to be near the desired characteristics, an optimization was completed to enhance the gain and efficiency of the structure. A transparent overview of the full design is shown in Figure 13c.

### Fabrication Using PCB and Foam Dielectric

Nominal boards were designed and fabricated for each of the two PCBs. The top PCB (which hosts the top-most patch) was fabricated in a batch job that provided three different patch sizes. This protected against the possibility that the antenna's operating frequency might shift during fabrication. The three different patch sizes had slightly different radiation characteristics so that the best option could then be assembled. Ultimately, the nominal/optimized patch size was selected based on the measured return loss, and the prototype was assembled with this top PCB. The quadrature hybrid couplers and the SMA feeds were populated and the boards were attached to mounting plates, at which point the boards were ready for characterization. The mounting plate serves as a ground plane for the antenna and also allows for the array to be attached structurally during testing and operation. Pictures of the front and back of a  $1 \times 4$  module are shown in Figure 14a.

Mounting plates were created to host multiple  $1 \times 4$  modules, allowing the antenna to be tiled to a  $4 \times 4$  or a  $1 \times 16$  geometry. Images of the antenna in these configurations are shown in Figure 14b. Note that the top patches reside on the back of the upper PCB and are not visible after assembly.

### Characterization Testing

To test the performance of the  $1 \times 4$ ,  $1 \times 16$ , and  $4 \times 4$  antenna configurations, each was measured in an anechoic chamber. Measurements were taken in

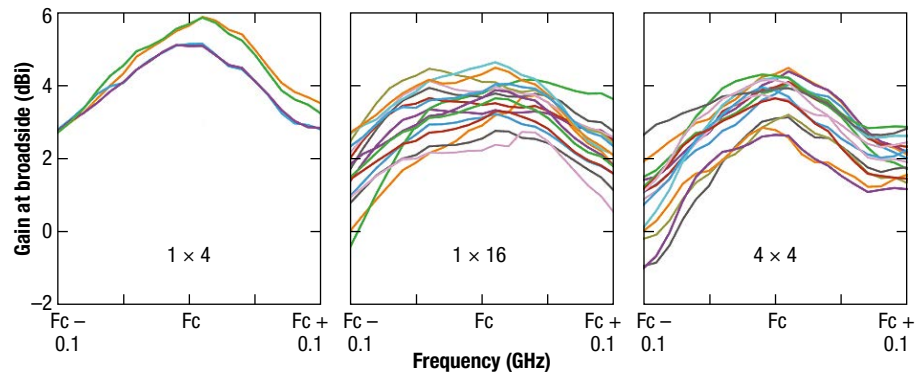


**Figure 15.** Antenna gain vs. frequency for  $1 \times 4$ ,  $1 \times 16$ , and  $4 \times 4$  geometries. Variation among the patches is attributed to their position within the array and the tolerances of the assembly/fabrication.

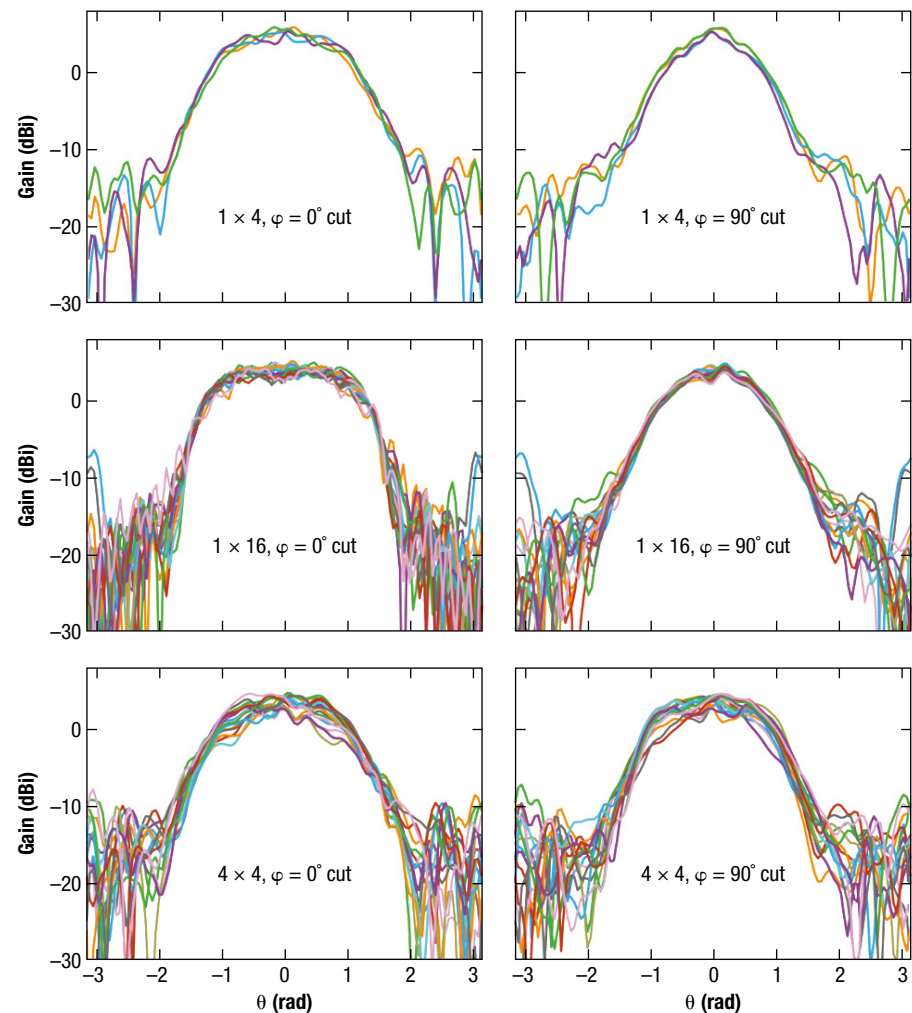


**Figure 16.** Major axes pattern measurements for  $1 \times 4$ ,  $1 \times 16$ , and  $4 \times 4$  geometries. The ripple in the radiation patterns is primarily driven by finite array effects and mutual coupling between the elements.

a spherical chamber, allowing for the pattern of each patch to be characterized independently. Gain as a function of frequency and angle could then be calculated. The right-hand circular polarization gain for each of the elements was found to be approximately 4–5 dB. The left-hand circular polarization gain was at least 8 dB below this. The gain at broadside is shown in Figure 15 for the geometries shown above. Variation among the patches is attributed to their position within the array and the tolerances of the assembly/fabrication.

Figure 16 shows pattern measurements for the major axes for the three geometries, which include some ripple in the radiation patterns. This is primarily driven by finite array effects and mutual coupling between the elements.

## RF ELECTRONICS DEVELOPMENT AND PROTOTYPING

The RF electronics design provides the FMPA receiver system analog front end, which performs the following functions:

- Low-noise amplification and filtering
- Programmable, coherently ganged frequency references
- Channel downconversion to an intermediate frequency (IF)
- $N$  channel analog combining
- User interface and control via the main controller board and controller firmware

The RF electronics consist of a set of 16 frequency downconverters that take in the RF signal and downconvert it to an IF of 500 MHz. The 16 IF signals from each antenna element are then stacked into a frequency comb whose spacing and bandwidth are chosen based on the properties of the signals of interest and the SDR's instantaneous bandwidth. A high-level block diagram of the RF electronics including the antennas and combiner is shown in Figure 17.

The input of each downconverter is designed to directly interface with antenna elements, like in a phased array. Thus, the design is optimized to keep the noise figure low and attain the highest possible dynamic range. This, the

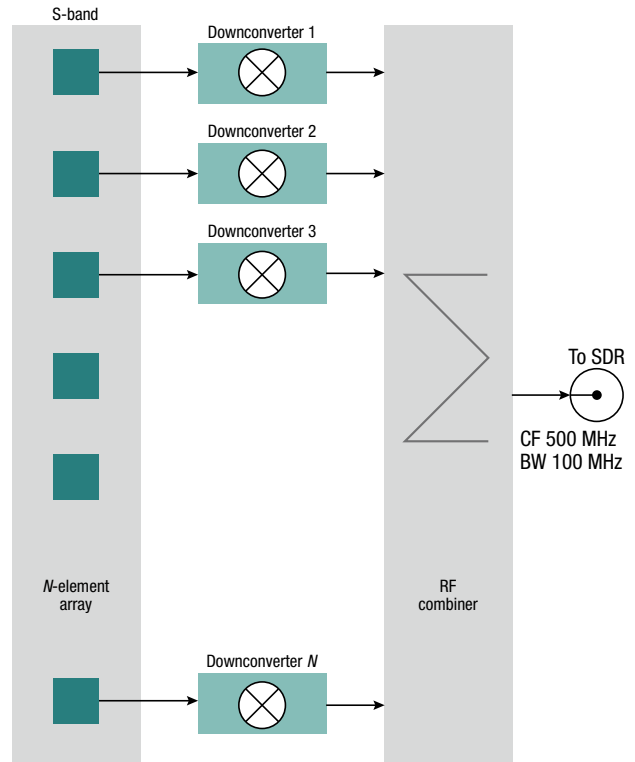


**Figure 17.** Block diagram of the RF electronics. The electronics include the antenna array, 16 frequency downconverters, and an RF combiner.

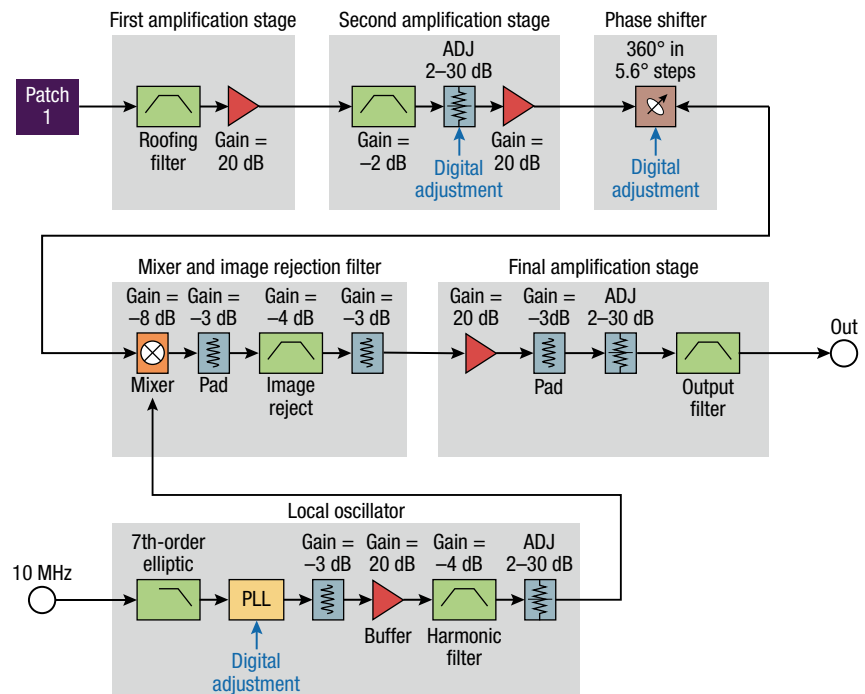


**Figure 18.** Block diagram of the downconverter block. The downconverter block consists of multiple amplification stages, a phase shifter stage, mixer and image rejection stages, and a local oscillator (LO). PLL, phase-locked loop. ADJ, adjustable attenuator.

first iteration of the design, used high-dynamic-range active amplifiers. It was optimized for RF performance rather than low power operation. The hardware was designed to prove the FMPA concept. After RF parameters are well established, the design will be improved for other variables such as power efficiency, overall size, and weight. The overall block diagram for the downconverter block is shown in Figure 18.

Each downconverter is phase locked to a signal reference at 10 MHz, making the entire system phase coherent. The downconverter output frequency is programmable and intermediate RF filtering allows the output of each downconverter to operate in a bandwidth of  $\sim 100$  MHz centered at 500 MHz.

### Front End

The front end consists of two amplification stages. The first amplification stage of the downconverter includes a surface acoustic wave (SAW) roofing filter. Inputs are protected by high-impedance paths to wick off static charge, thereby protecting against electrostatic discharge. The filter is followed by a low-noise amplifier (LNA), TQL9093 made by Quorvo, that has a high third-order intercept point. This LNA provides a low noise figure and has a proven track record of robustness and a low failure rate. The power to the LNA is well regulated and clamped at 5 V using transient voltage suppressor (TVS) diodes (Figure 19).

The second amplification stage provides a second stage of filtering that uses the same SAW device as the roofing filter used in the first amplification stage. The output from the SAW filter is gain-leveled using a digitally controlled attenuator. The attenuator is followed by another LNA, providing an approximate gain of 20 dB. The digitally controlled attenuator is adjusted as needed based on operational requirements to provide sufficient gain.

By providing adjustable gain between the first and second amplification stages, the input-intercept-point and overall system noise figure can be balanced. For instance, in an airborne application, the achievable SNRs for different scenarios could vary greatly. Thus, a system designed with agile gain is likely to be more suitable to such applications.

The second amplification stage feeds a phase shifter

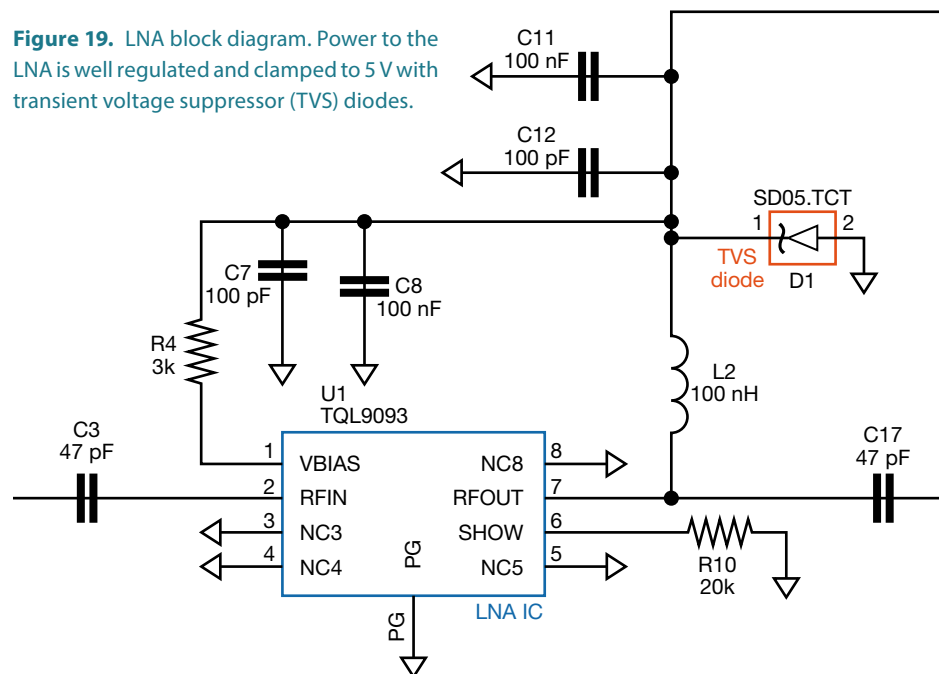
integrated circuit (IC) made by Macom (MAPS-010163). This IC provides  $360^\circ$  of phase shift, adjustable with a granularity of  $5.6^\circ$ . This flexibility allows the downconverter to also be used in a standard phase array configuration if needed. In such a case, a single fixed IF frequency is used for all elements, and beams are formed by adjusting the phase and amplitude for each individual element. Phase adjustment is also possible via the phase-locked loop (PLL).

### Mixer and Image Reject Filter

A downconverter's critical task is mixing down the signal of interest to an IF. Selecting the proper mixer is key to achieving good dynamic range and shutting down spurious signal generation at the source. For this task, the ADE-42MH+ was selected. The achievable insertion loss and the third-order intercept region for a given a local oscillator (LO) injection level were of particular interest. It was discovered that high LO levels tended to couple and contaminate the circuitry, contributing to high levels of spurious signal generation. An important objective for the FMPA was to design each downconverter to be reasonably small in size.

The FMPA RF electronics system consists of multiple downconverters with their outputs combined. Each converter has large signal gain. In essence, each downconverter is a very sensitive receiver, and in this particular design implementation, 16 converters are physically close to one another. Furthermore, their outputs are summed using combiners, and they have common DC power distribution circuitry along with digital control. During initial breadboarding, stray signals that were either radiated or conducted managed to be ingested via one of these

**Figure 19.** LNA block diagram. Power to the LNA is well regulated and clamped to 5 V with transient voltage suppressor (TVS) diodes.



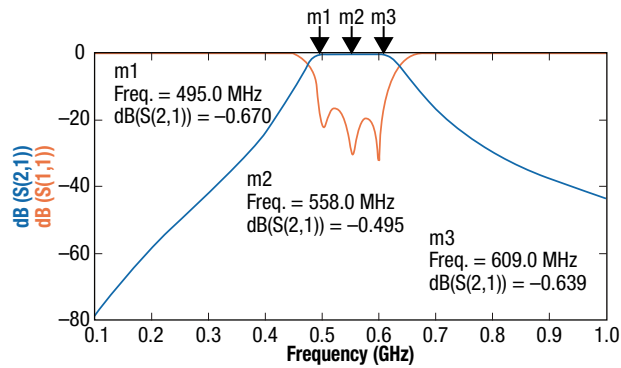


**Figure 20.** Post-mixer image rejection filter response. The filter was implemented as a seventh-order elliptic filter, and the design was simulated and bench-adjusted for optimal rejection of LO and other spurious signal leakage.

paths, creating excessive spurs in the pass band. Filtering carefully, selecting proper parts, and adjusting signal levels such as mixer LO became critical. Modeling these performance metrics into submission was nearly impossible, so bench testing and careful circuit design at every stage helped minimize these effects.

The post-mixer image rejection filter was implemented as a seventh-order elliptic filter. The filter design was simulated and bench-adjusted for optimal performance in terms of rejecting LO and other spurious signal leakage. The filter was modeled in Keysight Technologies ADS to establish the expected performance; the simulated filter response is shown in Figure 20.

### Final Amplification Stage, Gain Control, and Filtering

The final amplification stage follows the mixer and image rejection filter. The amplifier gain is 20 dB. Gain balancing is accomplished by fixed attenuator pads. These attenuator values were chosen through simulation to ensure that this gain stage was stable and had a stability factor of  $K > 1$  for all conditions.  $\mu$  and  $\mu$ -prime, also metrics of stability, were designed to be  $>1$  between 0 and 1 GHz, ensuring unconditional stability. Between the stages, gain padding ensures stability. Gain leveling at the final output is fine-tuned using a manually adjusted voltage controlled attenuator.

### Local Oscillator

The LO uses a high-performance PLL with desirable characteristics such as high-resolution step size, low phase noise, low spurious levels, and high endurance to interference. Analog Devices' ADF4351 was chosen and employed as the core of the LO circuit.

The reference frequency required is 10 MHz at 0 dBm. The reference signal is fed via a seventh-order elliptic low-pass filter into the ADF4351. The filter has aggressive transmission zeros that extend the out-of-band

rejection to over 80 dB for frequencies beyond 100 MHz. This level of rejection is required to circumvent reverse feedback, a phenomenon when signals within the PLL are parasitically fed back into the 10-MHz source, potentially compromising the spectral integrity of the 10-MHz source. The output of the PLL is buffered via fixed attenuators and then amplified to further enhance buffering. The buffering permits the LO signal to be set to the optimal amplitude for the mixer operation.

### Integration and Assembly of RF Electronics

To realize this novel architecture and enable its evaluation in real-world conditions, electro-mechanical packaging experts in APL's Research and Exploratory Development Department (REDD) were engaged to develop a suitable enclosure for both the single-channel downconverter and a package that integrated up to 16 discrete channel downconverters. Configurability and ruggedness were essential to enable ground testing at an outdoor range and, subsequently, integration and testing aboard an airborne platform.

The downconverter electronics for processing a single antenna channel are integrated onto a single PCB and packaged into an individual aluminum enclosure for electromagnetic interference shielding. The single antenna channel downconverter assembly is shown in Figure 21, along with the fully integrated 16-channel FMPA assembly.

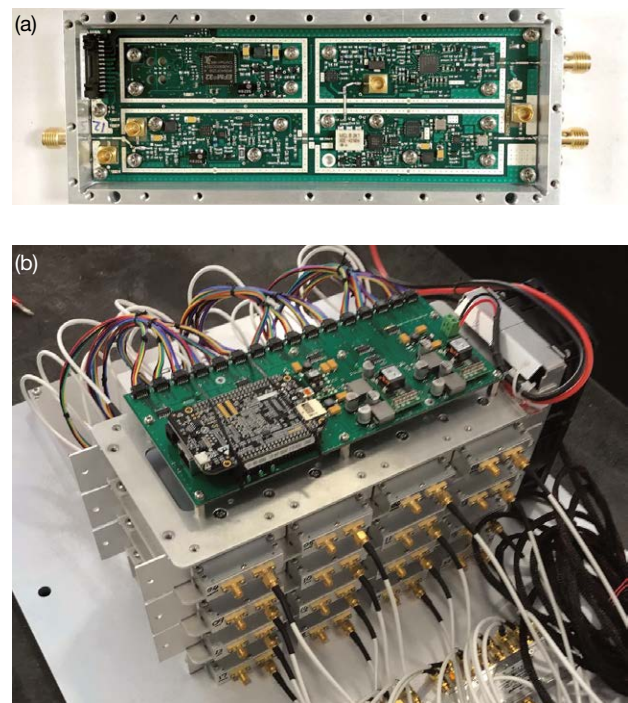


**Figure 21.** Downconverter electronics. (a) A single antenna channel and (b) a fully integrated RF electronics assembly for 16 channels.

To ensure that the analog domain achieves the required performance before signal digitization, several technical challenges had to be overcome in the RF electronics design. REDD's RF characterization, modeling, and design experts were engaged since they are uniquely suited to this challenge. Specifically, the following design aspects had to be optimized:

- Low-noise amplification maximizing dynamic range and minimizing noise figure
- LOs with high spectral integrity and minimized contamination of adjacent channel LOs
- High-signal-gain channel mixing while suppressing crosstalk-induced spurs and intermodulation
- Channel filtering prior to  $N$  channel combining (Implementing high-performance narrowband channel filtering was deferred to a subsequent development effort to spare the expense of custom filters. This was done with the understanding that for this prototype, the ultimate phased-array SNR gain would be negated by the wideband noise accumulation during  $N$  channel combining.)

Because this was a proof of concept, SWaP was a lower priority than functionality and performance. Reducing SWaP will be a priority in a follow-on effort.

## CONTROL INTERFACE AND SIGNAL PROCESSING

The  $N$  channel frequency-multiplexed analog output of the RF electronics feeds an SDR. In a production system, the signal processing would be performed in real time within the SDR's processor and field-programmable gate arrays. For this effort, the signal processing was performed in non-real time in MATLAB running on a PC.

- An Ettus E310 SDR collected and recorded raw RF complex samples.

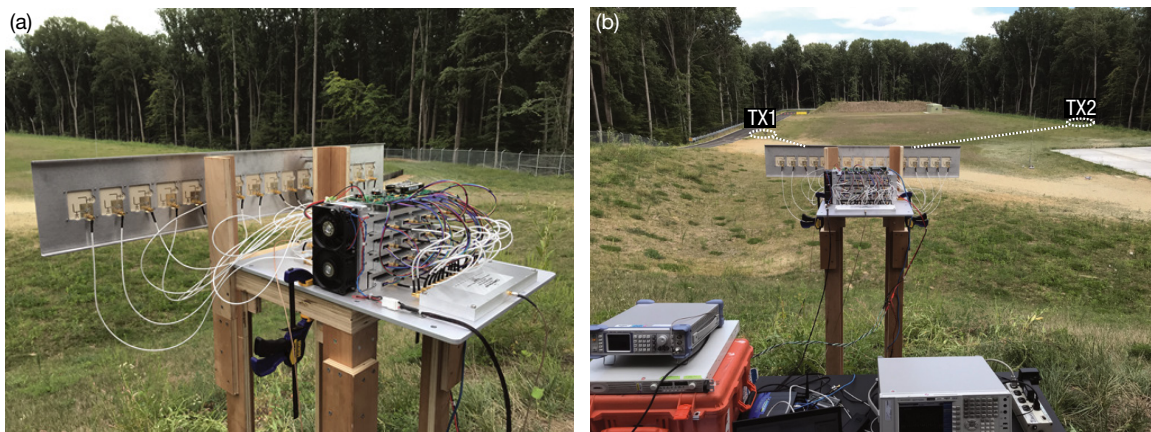
- An APL-developed software graphical user interface communicated to the main controller board and the Ettus E310 SDR and controlled FMPA system operation during functional testing.
- APL-developed MATLAB batch processing code implemented the FMPA signal processing algorithms developed for the FMPA test bed. This code was then used to postprocess the raw RF data captured and recorded during FMPA system test events.

## FMPA ANTENNA RANGE TEST

The FMPA system, configured as a  $16 \times 1$  array, was tested in a static environment on an antenna range located on APL's main campus in Laurel, Maryland. The range test was the first time the FMPA system was deployed to collect RF signals, so the focus was on verifying the FMPA's ability to beam steer and isolate RF emissions from physically separated transmitters. Figure 22 shows the FMPA system as it was deployed for the range test.

Two transmitters, TX1 and TX2, were placed on the range at the distances and azimuth angles from the FMPA broadside (Table 1). Both transmitters were turned on, and they transmitted CW with TX1 tuned at a frequency 50 kHz above TX2.

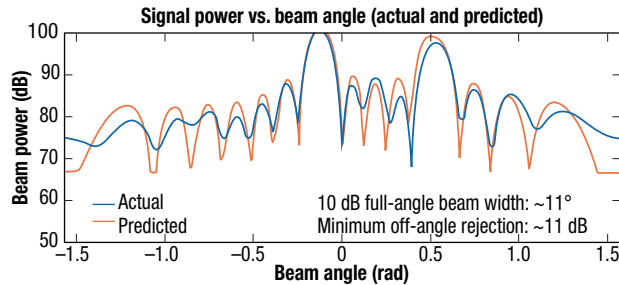
The FMPA system collected and recorded raw RF quadrature (IQ) data after the signals were received by the 16 antenna elements and formed into a single 16-channel frequency-multiplexed data stream. The FMPA's performance was evaluated after signal collection in postprocessing analysis. The recorded frequency-multiplexed data were run through the FMPA signal processing chain for 128 iterations, with each iteration using a different set of beam coefficients so that the beam was effectively swept across azimuth angles from  $-\pi/2$  rad to  $+\pi/2$  rad in 128 steps.



**Figure 22.** Range test configuration of FMPA system. (a) FMPA configured on a test stand. (b) Transmitter (TX1 and TX2) deployment on the range relative to the FMPA system.

**Table 1.** Physical placements of TX1 and TX2 relative to FMPA system

Transmitter	Azimuth Angle (rad)	Distance (m)
TX1	-0.125	79
TX2	0.512	83
FMPA	0.000	0

**Figure 23.** Formed-beam signal response as beam is swept from  $-\pi/2$  to  $+\pi/2$  rad in 128 steps. The orange trace is the normalized response predicted by theory, and the blue trace is the normalized FMPA-measured response.

In Figure 23, the blue trace shows the normalized FMPA response received from TX1 and TX2 as a function of the beam being swept from left to right ( $-\pi/2$  to  $+\pi/2$  rad). The orange trace shows the normalized predicted response. This test verified the basic functionality of the FMPA system, demonstrating its ability to provide directed gain at a desired look angle while simultaneously providing reduced sensitivity (or isolation) at undesired look angles.

## FMPA FLIGHT TEST

In preparation for the flight test, the interface hardware that mounted the system aboard the Cessna Caravan test aircraft was designed and fabricated in-house. APL's engineering team has extensive experience

mounting similar systems aboard certified airframes and, if necessary, can provide comprehensive stress, flow, and thermal modeling and analysis of such systems to ensure compliance with aircraft operating parameters. Given the system's internal mounting, low power, and light weight, the installation required minimal evaluation. The system was integrated into the belly pod of the Caravan by REDD and Asymmetric Operations Sector (AOS) staff members.

The FMPA system, configured as a  $16 \times 1$  array, was flight-tested on a Cessna Caravan aircraft in the vicinity of Hagerstown, Maryland. The flight test verified FMPA system performance over a wide range of transmitter-to-receiver geometries. The installation of the FMPA system onto the Cessna Caravan aircraft is shown in Figure 24.

The test aircraft flew in a counterclockwise direction, as shown in Figure 25, around three ground-based transmitters, TX1, TX2, and TX3, at a speed of 160 kt with a 4-nautical-mile (NM) radius from TX1, at an altitude of 10 kft. TX1, TX2, and TX3 were separated in frequency to enable independent analysis of coherent gain and off-beam rejection for each of the three locations. The antenna array was installed on the left-facing side of the aircraft and thus was always pointing its broadside vector nominally at the center of the orbit at TX1.

Like during the range test, during the flight test the FMPA system collected and recorded raw RF quadrature (IQ) data after the signals were received by the 16 antenna elements and formed into a single 16-channel frequency-multiplexed data stream. The FMPA's performance was evaluated after signal collection in post-processing analysis. For the flight test, the data were analyzed at each  $30^\circ$  step in aircraft position around the orbit. For each step, the recorded frequency-multiplexed data were run through the FMPA signal processing chain for 128 iterations, with each iteration using a different set of beam coefficients so that the beam was effectively swept across azimuth angles from  $-\pi/2$  rad to  $+\pi/2$  rad in 128 steps.

**Figure 24.** FMPA installation into the hold of a Cessna Caravan. (a) The electronics assembly and (b) the 16:1 linear antenna array.

At each 30° step, the FMPA’s performance was evaluated for each of the three transmitters in terms of (1) average single antenna channel SNR, (2) on-target formed-beam SNR gain, and (3) off-beam target signal rejection. The on-target formed-beam SNR gain is predicted by theory to be 12 dB [10log<sub>10</sub>(16)]. The off-beam rejection is predicted to be at least -13 dB to the first sidelobe (an antenna taper was not used).<sup>4</sup> The results of the FMPA performance are shown in Table 2.

These results demonstrate that the FMPA generally performed as expected across a wide range of beam angles. The beam angle for TX1 was held nominally at 0 rad, while the beam angles for TX2 and TX3 varied over the course of the orbit. The beam angles for TX3 achieved the greatest magnitudes, with a range from -0.760 to +0.795 rad. Across the

range of beam angles, the beam SNR gain was nominally 12 dB, as predicted; however, there was significant variability that increased with transmitter placement angle further from array broadside. Similarly, the average off-beam rejection was typically better than 13 dB



Figure 25. Satellite view of the Hagerstown area with overlays indicating circular flight path (green) and the three transmitter locations (magenta). (Map data © 2020 Google.)

Table 2. FMPA flight test results

Time Stamp	Wall Clock	Broadside Angle (rad)			Average Channel SNR (dB)			Beam SNR Gain (dB)			Average Off-Beam Rejection (dB)		
		TX1	TX2	TX3	TX1	TX2	TX3	TX1	TX2	TX3	TX1	TX2	TX3
8/9/2020 15:55:08	1:00	-0.021	0.356	-0.374	64.8	55.8	53.1	11.9	12.7	11.2	-21.6	-20.7	-23.6
8/9/2020 15:56:12	12:00	-0.015	0.516	-0.105	64.3	53.8	41.9	11.3	11.5	10.1	-9.4	-16.1	-5.0
8/9/2020 15:57:23	11:00	0.004	0.552	0.193	62.0	69.1	55.0	11.2	11.3	10.7	-16.7	-19.8	-16.4
8/9/2020 15:58:23	10:00	0.007	0.294	0.420	57.2	69.8	50.9	10.0	7.1	11.0	-19.3	-17.4	-11.2
8/9/2020 15:59:01	9:00	0.005	-0.038	0.552	63.5	64.6	58.6	11.6	7.1	11.0	-1.3	-16.7	-23.2
8/9/2020 15:59:47	8:00	0.017	-0.396	0.711	64.7	67.5	50.6	12.2	11.8	10.7	-26.1	-16.7	-21.8
8/9/2020 16:00:38	7:00	0.020	-0.551	0.795	65.3	57.7	64.6	11.7	10.0	11.6	-21.8	-18.5	-28.2
8/9/2020 16:01:36	6:00	0.039	-0.475	0.491	64.1	48.5	61.7	11.4	7.1	4.0	-15.6	-17.9	-18.0
8/9/2020 16:02:26	5:00	0.035	-0.330	-0.386	65.4	52.3	71.0	11.5	11.2	4.8	-16.9	-5.1	-23.8
8/9/2020 16:03:13	4:00	0.032	-0.158	-0.760	66.2	51.6	65.6	10.9	9.7	10.8	-15.0	-19.3	-13.9
8/9/2020 16:04:07	3:00	0.005	0.028	-0.731	69.4	52.9	53.7	11.8	10.8	9.4	-2.2	-6.2	-27.5
8/9/2020 16:04:53	2:00	-0.022	0.173	-0.597	64.9	43.3	47.7	11.1	9.2	7.3	-14.4	-12.5	-16.9
8/9/2020 16:05:47	1:00	-0.032	0.343	-0.387	62.1	53.5	47.5	10.0	10.3	9.3	-25.2	-15.2	-16.7
8/9/2020 16:06:52	12:00	-0.018	0.514	-0.107	63.4	55.3	45.5	11.4	10.7	11.2	-9.8	-22.7	-4.0
8/9/2020 16:08:02	11:00	0.010	0.557	0.196	60.9	72.3	40.6	10.9	10.1	10.7	-15.9	-26.4	-13.2
8/9/2020 16:09:01	10:00	0.014	0.305	0.424	58.5	70.4	47.9	9.1	7.9	9.5	-21.4	-14.5	-10.1
8/9/2020 16:09:40	9:00	0.011	-0.044	0.563	65.9	60.4	55.8	11.7	7.7	10.4	-2.4	-16.7	-20.8
8/9/2020 16:10:21	8:00	0.012	-0.382	0.698	64.2	70.1	53.1	11.9	11.2	10.3	-27.9	-20.8	-20.0
8/9/2020 16:11:14	7:00	0.009	-0.560	0.788	65.0	62.5	57.9	12.1	9.4	11.0	-20.0	-18.5	-25.3
8/9/2020 16:12:11	6:00	0.022	-0.496	0.505	62.5	38.1	54.7	12.2	5.8	0.3	-15.2	-5.4	-14.6

below the peak, but with variability across the range of beam angles. Further investigation is required to determine the source of variability for these results.

## POTENTIAL FUTURE WORK

One potential benefit of the FMPA is the possibility for a low-cost, compact phased-array antenna kit that serves as an add-on component to existing SDR installations. To realize this benefit, the SWaP and complexity of the per-channel FMPA analog electronics need to be reduced. Furthermore, an advantage of these per-channel analog components over the ADC and digital bus multiplexing electronics of an equivalent digital multiplexing scheme has to be shown. An investigation into reduced-SWaP analog electronics could be coupled with a repackaging exercise to determine whether a portable FMPA kit is viable and cost effective, with anticipated applicability to many existing single-channel SDR installations.

We briefly mentioned that the design could also operate as a CMCT. We hope to further explore this capability. One implementation might use CMCT capabilities to quickly scan for energy across a wide swath of the RF spectrum and then switch modes to the FMPA capability for increased directivity and interference rejection. Another implementation might use the CMCT transmit capability to concurrently broadcast  $N$  independent data streams on  $N$  unique frequencies.



**Spyro Gumas**, Asymmetric Operations Sector, Johns Hopkins University Applied Physics Laboratory, Laurel, MD

Spyro Gumas is a project manager and technical lead in APL's Asymmetric Operations Sector. He has a BS and an MS in electrical engineering, both from the Georgia Institute of Technology. He has extensive background in digital signal processing, electronics design, and software development in the fields of radio frequency communications, acoustics, radar, fiber optic communications, mobile satellite telephony, spaceborne infrared image processing, and graphics processing. Spyro has managed development teams as an engineering manager, technical lead, project manager, and program manager. His email address is [spyro.gumas@jhuapl.edu](mailto:spyro.gumas@jhuapl.edu).



**Ravi P. Goonasekeram**, Research and Exploratory Development Department, Johns Hopkins University Applied Physics Laboratory, Laurel, MD

Ravi P. Goonasekeram is a member of the Principal Professional Staff and a chief scientist in APL's Research and Exploratory

## CONCLUSION

An APL team developed and demonstrated an FMPA to validate a new type of phased-array antenna system whereby the individual antenna channels are frequency-multiplexed onto a single analog channel, which then feeds a conventional single-channel digital transceiver. The demonstration validated the approach and verified that the FMPA would perform similarly to more traditional phased-array implementations. Future work will seek to reduce SWaP and add a phased-array transmit capability. APL's integrated capabilities and cross-organizational collaboration were key in the demonstrated technical success of this project, which was completed in less than a year.

The FMPA has been demonstrated as a viable and practical alternative implementation for phased-array antenna systems, offering capabilities in applications where phased arrays might otherwise not be practical. The inherent ability for the FMPA system to double as a CMCT further increases its flexibility and expands its potential applications.

## REFERENCES

- <sup>1</sup>M. Skolnik, *Introduction to Radar Systems*. New York, NY: McGraw-Hill, 1980, p. 278.
- <sup>2</sup>E. Brookner, Chapters 20 and 21, in *Radar Technology*. Norwood, MA: Artech House, 1978.
- <sup>3</sup>M. Skolnik, *Radar Handbook*, 2nd ed. New York, NY: McGraw-Hill, 1990, p. 7.8.
- <sup>4</sup>E. Brookner, *Practical Phased Array Antenna Systems*. Norwood, MA: Artech House, 1997, p. 2.14.

Development Department. He has a BS in mathematics/applied mathematics from Washington Adventist University and over 25 years of theoretical and practical radio frequency (RF) experience in microwave circuit design from the HF through the Ka band. Ravi's interests are high-power RF amplifier design/linearization techniques, ultralow-noise phase-locked loop design, low-noise RF front ends, novel transceiver architectures, and microwave filter design and modeling. His research interests include using unusual synthesis techniques for broadband power amplifier design and modeling. Ravi's designs have been deployed in various signals intelligence, electronic intelligence, nontraditional localization, electronic attack, and warfare systems. His email address is [ravi.goonasekeram@jhuapl.edu](mailto:ravi.goonasekeram@jhuapl.edu).



**Timothy A. Sleasman**, Research and Exploratory Development Department, Johns Hopkins University Applied Physics Laboratory, Laurel, MD

Timothy A. Sleasman is a research scientist in APL's Research and Exploratory Development Department. He has a BS in physics and a BS in mathematics from Boston College and a PhD in electrical and computer engineering from Duke University. His interests primarily focus

on the study of electromagnetic waves and how they interact with matter, including novel devices for controlling waves holographically and the design of dynamic aperture antennas. Of particular interest are the application of electromagnetic manipulation in communications platforms, computational imaging and inverse problems, and synthetic aperture radar and radar absorbing material. He has extensively studied holographic metasurface apertures across these various contexts with the goal to enhance size, weight, and power characteristics and has provided a framework to design and optimize such devices. He is a member of the IEEE Antenna and Propagation Society. His email address is [timothy.sleasman@jhuapl.edu](mailto:timothy.sleasman@jhuapl.edu).



**John A. Marks**, Research and Exploratory Development Department, Johns Hopkins University Applied Physics Laboratory, Laurel, MD

John A. Marks is a mechanical and electronics packaging engineer in APL's Research and Exploratory Development Department. He has a BS in mechanical engineering from Villanova University. John has 38 years of mechanical design experience in electronics packaging, including in space, airborne, ground, shipboard, and office environments, as well as in investment and die castings, electromagnetic interference/radio frequency interference protection, thermal, plastic encapsulated components, multilayer printed wiring boards (PWBs), rigid-flex PWBs, surface mount, coefficient of thermal expansion (CTE)-matched designs, multichip module design, flex cables, shock, vibration, thermal and stress analysis, electromechanical power supplies, and

material selection. His designs include the use of aluminum and composite and rapid prototyping materials to limit weight in weight-sensitive programs. His email address is [john.marks@jhuapl.edu](mailto:john.marks@jhuapl.edu).



**David W. Elsaesser**, Laboratory for Physical Sciences, Department of Defense, College Park, MD

David W. Elsaesser is a research physicist at the Laboratory for Physical Sciences (LPS), Department of Defense. He received a BS degree in physics from Xavier University and MS and PhD degrees from the Air Force Institute of Technology in engineering and materials physics, respectively. As an officer in the US Air Force (USAF), David conducted research in electrical and optical properties of III-V electronic materials, including, GaAs, AlGaAs, and InP, and did dissertation-related work on rare-earth doped III-Vs. He went on to lead a program in the acquisition and modeling of radar and infrared/electro-optics signatures on US military aircraft and parametric data on US communications and radar systems in support of operational warning, vulnerability analyses, and countermeasures development. As a field-grade officer, he managed national-level tactical signals intelligence and cryptologic research programs. Upon retiring from the USAF, David joined LPS, where he worked on development of low-power transceivers, infrared and radio-frequency (RF) geolocation technologies, and embedded control of RF circuits. He is now developing and characterizing materials and fabrication technologies for additive manufacturing and printed electronics. His email address is [dwelsae@lps.gov](mailto:dwelsae@lps.gov).



A group photo of the team taken in Hagerstown, Maryland, the day of the flight test. From left to right: Ravi Goonasekeram, Tim Sleasman, John Marks, Mike Montgomery, Gary Letsch, Dave Elsaesser, and Spyro Gumas.